



The Puzzling Properties of the MACS1149-JD1 Galaxy at $z = 9.11$

Massimo Stiavelli¹, Takahiro Morishita², Marco Chiaberge^{3,4}, Claudio Grillo^{5,6}, Nicha Leethochawalit⁷,
Piero Rosati^{8,9}, Stefan Schuldt^{5,6}, Michele Trenti^{10,11}, and Tommaso Treu¹²

¹Space Telescope Science Institute, 3700 San Martin Drive, Baltimore, MD 21218, USA

²IPAC, California Institute of Technology, MC 314-6, 1200 E. California Boulevard, Pasadena, CA 91125, USA

³Space Telescope Science Institute for the European Space Agency (ESA), ESA Office, 3700 San Martin Drive, Baltimore, MD 21218, USA

⁴The William H. Miller III Department of Physics and Astronomy, Johns Hopkins University, Baltimore, MD 21218, USA

⁵Dipartimento di Fisica, Università degli Studi di Milano, Via Celoria 16, I-20133 Milano, Italy

⁶INAF—IASF Milano, via A. Corti 12, I-20133 Milano, Italy

⁷National Astronomical Research Institute of Thailand (NARIT), Mae Rim, Chiang Mai, 50180, Thailand

⁸INAF—OAS, Osservatorio di Astrofisica e Scienza dello Spazio di Bologna, via Gobetti 93/3, I-40129 Bologna, Italy

⁹Dipartimento di Fisica e Scienze della Terra, Università degli Studi di Ferrara, Via Saragat 1, I-44122 Ferrara, Italy

¹⁰School of Physics, University of Melbourne, Parkville 3010, VIC, Australia

¹¹ARC Centre of Excellence for All Sky Astrophysics in 3 Dimensions (ASTRO 3D), Australia

¹²Department of Physics and Astronomy, University of California, Los Angeles, 430 Portola Plaza, Los Angeles, CA 90095, USA

Received 2023 August 27; revised 2023 September 28; accepted 2023 October 8; published 2023 November 3

Abstract

We analyze new JWST NIRCam and NIRSpect data on the redshift 9.11 galaxy MACS1149-JD1 (hereafter JD1). Our NIRCam imaging data reveal that JD1 comprises three spatially distinct components. Our spectroscopic data indicate that JD1 appears dust free but is already enriched, $12 + \log(\text{O}/\text{H}) = 7.90^{+0.04}_{-0.05}$. We also find that the carbon and neon abundances in JD1 are below the solar abundance ratio. Particularly the carbon under-abundance is suggestive of recent star formation where Type II supernovae have already enriched the interstellar medium (ISM) in oxygen but intermediate mass stars have not yet enriched the ISM in carbon. A recent burst of star formation is also revealed by the star formation history derived from NIRCam photometry. Our data do not reveal the presence of a significant amount of old populations, resulting in a factor of $\sim 7\times$ smaller stellar mass than previous estimates. Thus, our data support the view that JD1 is a young galaxy.

Unified Astronomy Thesaurus concepts: [High-redshift galaxies \(734\)](#)

1. Introduction

The high sensitivity of the NIRSpect spectrometer on board JWST (Böker et al. 2023) has enabled us to study emission-line diagnostics of galaxies at redshift $z > 8$ with unprecedented detail. Already the Early Release Observations (ERO) observations of SMACS J0723.3-7327 S04590 at $z = 8.496$ (Curti et al. 2023; Heintz et al. 2023) enabled the first detection at high redshift of the auroral line $[\text{O III}]\lambda 4363$ and its use to derive an electron temperature $T_e \geq 24,000$ K. The derived metallicity for this object is $12 + \log(\text{O}/\text{H}) \sim 7$. Comparison with strong emission-line diagnostics showed that this object was outside the validity range of most calibrations. A broader look at a small sample of objects with auroral lines by Laseter et al. (2023) and Sanders et al. (2023) finds that abundances derived from the T_e method are generally not consistent with those from locally calibrated, strong emission lines.

The galaxy MACS1149-JD1 (hereafter JD1; Zheng et al. 2012) was one of a handful of confirmed redshift greater than nine galaxies known before the launch of JWST and, being substantially lensed, it was a credible candidate for searching for a potentially very low-metallicity protogalaxy. The high-redshift nature of MACS1149-JD1 was confirmed thanks to Atacama Large Millimeter Array (ALMA) detection of $[\text{O III}]\lambda 88 \mu\text{m}$ (Hashimoto et al. 2018; Tokuoka et al. 2022). The previous measurements by Spitzer indicate the presence of old

stellar populations, making it a relatively massive system among other galaxies at similar redshifts. These exceptional properties of JD1 led us to make it as one of the prime candidates for deep spectroscopy with JWST.

It is worth noticing that another bright, pre-JWST high- z galaxy, GN-z11 (Oesch et al. 2016), while extremely interesting (see, e.g., Bunker et al. 2023; Cameron et al. 2023a; Charbonnel et al. 2023; Maiolino et al. 2023; Tacchella et al. 2023), is considered to possibly host an active galactic nucleus (AGN) and is at a redshift where $[\text{O III}]\lambda 5007$ is beyond the NIRSpect sensitivity range and therefore makes it less likely for us to be able to carry out a direct metallicity measurement using the auroral lines. As such, JD1 is currently one of a few luminous galaxies at $z > 9$ that allow a reliable auroral line analysis.¹³

In this paper, we present a comprehensive analysis of the properties of JD1 based on new observations by JWST. We describe our data on JD1 in Section 2. Section 3 derives the $\text{H}\beta$ -based star formation rate (SFR). Section 4 is devoted to deriving an estimate for dust extinction and presence of dust as well as constraints on the electron density. Section 5 derives the metallicity of JD1 through the direct method based on auroral lines and discusses implications from the other lines. Section 6 discusses the nonsolar abundance ratios for JD1. The star formation history and stellar mass are described in Section 7. Section 8 discusses our conclusions.

Original content from this work may be used under the terms of the [Creative Commons Attribution 4.0 licence](#). Any further distribution of this work must maintain attribution to the author(s) and the title of the work, journal citation and DOI.

¹³ Boyett et al. (2023) recently reported Gz9p3, another luminous galaxy at $z = 9.3$, which appears to be interacting and star forming. Unfortunately, the observations did not cover the $\text{H}\beta$ and $[\text{O III}]$ lines, preventing us from conducting a comparable analysis.

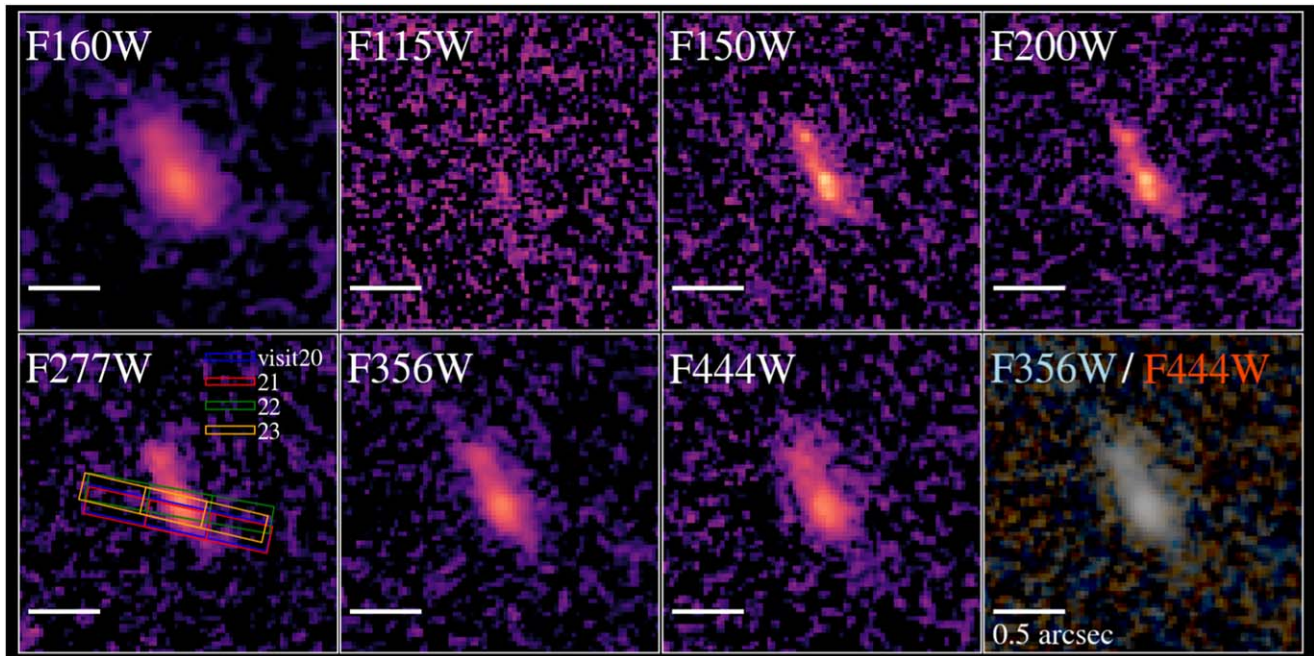


Figure 1. Stamp images of MACS1149-JD1 in HST F160W and NIRCams filters ($2''.4 \times 2''.4$). The MSA slits of the four visits (#20–23) are overlaid in the F277W stamp image. The pseudo two-color image using the F356W (blue) and F444W (red) filters, which corresponds to the Balmer break, is shown (right bottom).

Throughout the paper, we adopt the AB magnitude system (Oke & Gunn 1983; Fukugita et al. 1996); cosmological parameters of $\Omega_m = 0.3$, $\Omega_\Lambda = 0.7$, and $H_0 = 70 \text{ km s}^{-1} \text{ Mpc}^{-1}$; and the Chabrier (2003) initial mass function. We express all measurements as a function of $\mu/10$ where relevant.

2. Data and Analyses

2.1. NIRCams Photometry

NIRCams imaging observations (GTO #1199) were executed on June 6–8, 2023, with six filters configured (F090W, F115W, F150W, F200W, F277W, F356W, and F444W), with ~ 1.1 hr exposure each. We conduct photometry on the newly taken NIRCams images, along with the archival HST images that were originally taken in several HST programs (CLASH, HFF, GLASS, and BUFFALO; Postman et al. 2012; Treu et al. 2015; Lotz et al. 2017; Kelly et al. 2018; Steinhardt et al. 2020). We follow the same procedure presented in Morishita & Stiavelli (2023) for the image reduction and photometry. We hereby provide a high-level description of our workflow: raw NIRCams images are reduced by using the official `jdweb` pipeline (ver1.10.0, with context `pmap #1069`; Bushouse et al. 2023), with several customized steps included to effectively remove artifacts and improve cosmic-ray rejection. The final drizzled images are aligned to the World Coordinate System of GAIA. Source fluxes are calculated by using `SExtractor` (Bertin & Arnouts 1996) in point-spread function (PSF)-matched images to the PSF of F444W in an aperture of $r = 0''.16$, reaching to 5σ limiting magnitude of ~ 27.9 – 28.8 mag.

The NIRCams images of JD1 (see Figure 1) reveal the presence of three main components, two of which are included in our NIRSpect Micro Shutter Array (MSA) slits (Section 2.2). This means that geometry might play a significant role in the interpretation of the observations. However, we do not observe significant color differences between these components, and therefore in our following analysis we will not consider them separately.

2.2. NIRSpect MSA Spectroscopy

Our NIRSpect observations were executed over four different visits. In the first two visits, #20 and #22, respectively, for G235M and G395M, were taken at position angle (PA) = 257.766° . In the second group of visits, the same grating pair was used but with a slightly different PA, namely PA = 259.660° for visit #21/G235M and PA = 256.766° for visit #23/G395M. Slightly offset pointings ensure that roughly the same area of JD1 is covered by all exposures.

We reduce the MSA spectra using `msaexp`¹⁴ (ver0.6.13), following the procedure presented in Morishita et al. (2023a; also, T. Morishita et al. 2023, in preparation). The two-dimensional sky background is estimated by nodding the stacked spectrum for 6 pixels, and then it is subtracted. The one-dimensional spectrum is optimally extracted (Horne 1986) by using the one-dimensional source profile derived from the two-dimensional stacked spectrum as weight. For the extracted one-dimensional spectrum, we fit each line of interest with a Gaussian after subtracting the underlying continuum spectrum, estimated by scaling the best-fit SED template (see Section 7). We note that our flux measurements include a small correction for absorption in the Balmer series, which are inferred by the stellar template of the best-fit SED model. The correction is 1% for H β , 3% for H γ , and 4% for H δ . For each line, the total flux is estimated by integrating the flux over the wavelength range of $2 \times \text{FWHM}$, the latter derived from the Gaussian fit. For the [O III]-doublet, we fix the ratio to 1:3 and adopt a single parameter for the widths of both lines. Lastly, we determined an aperture correction by scaling the difference between the continuum measured around individual spectral lines and the one inferred by the best-fit SED template. We find that this correction is well described by the slit-loss correction one derives for a perfectly centered source (NIRSpect MOS Operations Slit Losses in JDox 2016) rescaled by the factor

¹⁴ <https://github.com/gbrammer/msaexp>

Table 1
Observed Properties of JD1

Redshift and Line Flux Measurements	
z^a	9.114 ± 0.001
$H\beta_{\lambda 4861}$	375 ± 10
$H\gamma_{\lambda 4340}$	174 ± 6
$H\delta_{\lambda 4102}$	125 ± 6
$[O II]_{\lambda\lambda 3727,3729}$	110 ± 5
$[O III]_{\lambda 4363}$	59 ± 5
$[O III]_{\lambda\lambda 4959,5007}$	3764 ± 14
$[Ne III]_{\lambda 3869}$	154 ± 5
$C III]_{\lambda\lambda 1907,1909}$	139 ± 8
Physical properties	
$M_{UV} \text{ (mag)}$	$-19.33^{+0.01}_{-0.01} - 2.5 \log(10/\mu)$
$SFR_{H\beta}(M_{\odot} \text{ yr}^{-1})$	$5.9 \pm 0.2(10/\mu)$
$SFR_{SED}(M_{\odot} \text{ yr}^{-1})$	$3.37^{+0.07}_{-0.07}(10/\mu)$
$M_{*}(10^8 M_{\odot})$	$1.61^{+0.25}_{-0.23}(10/\mu)$
β_{UV}	$-2.20^{+0.01}_{-0.01}$
$A_V \text{ (mag)}$	[0.0]
$Z(Z_{\odot})$	[0.2]

Note.

^a Redshift measured for the $H\beta+[O III]_{\lambda\lambda 4959,5007}$ lines. Flux measurements are corrected for aperture loss and expressed in units of $10^{-21}(10/\mu) \text{ erg s}^{-1} \text{ cm}^{-2}$.

~ 2.36 we find for $H\beta$ and $[O III]$. This correction is applied to measured line fluxes. However, most of our results are relatively unaffected by this wavelength-dependent aperture correction. The aperture correction allows us to apply measurements such as the SFR to the whole galaxy. In what follows, when necessary, we adopt the redshift $z = 9.114$ obtained for the $H\beta+[O III]$ lines.

We have checked that the line ratios obtained in all visits are consistent. Therefore, in the following we coadd the spectra and focus our analysis on the combined spectra. The measured line fluxes are reported in Table 1 and the spectrum is shown in Figure 2.

3. Star Formation Rate

The measured flux in $H\beta$ gives us an estimate of the SFR in JD1. Following the same approach as Heintz et al. (2023), we assume the Case B ratio for $f_{H\alpha/H\beta} = 2.80$ for $T_e = 1.6 \times 10^4 \text{ K}$ as derived from the direct analysis described in Section 5. We derive the SFR as

$$SFR_{H\beta} = 5.5 \times 10^{-42} L_{H\beta} \times f_{H\alpha/H\beta} \text{ (erg s}^{-1}\text{)}. \quad (1)$$

From the measured $H\beta$ flux of $3.7^{+0.1}_{-0.1} \times 10^{-18} \text{ erg s}^{-1} \text{ cm}^{-2}$ and assuming a gravitational magnification factor $\mu = 10$ (Hashimoto et al. 2018),¹⁵ we obtain $SFR_{H\beta} = 5.9^{+0.2}_{-0.2}(10/\mu) M_{\odot} \text{ yr}^{-1}$. Note that this is the aperture-corrected value of the SFR (Section 2.2). The estimated $H\beta$ -based SFR is consistent with the one derived with $[O III] 88 \mu\text{m}$ ($4.2^{+0.8}_{-1.1}(10/\mu) M_{\odot} \text{ yr}^{-1}$; Hashimoto et al. 2018). Also, the estimate is roughly consistent with the one from our SED

¹⁵ The Grillo et al. (2016) model predicts a median magnification of 12^{+1}_{-5} at the position of JD1, where the $\pm 1\sigma$ values are obtained by extracting 200 random sets of parameter values from the Markov Chain Monte Carlo model chains.

analysis, $\sim 3.2(10/\mu) M_{\odot} \text{ yr}^{-1}$, derived from the rest-frame UV luminosity by following Morishita et al. (2023b).

Given the large uncertainties in the magnification values at the location of JD1 (e.g., Grillo et al. 2016; Finney et al. 2018) and the relative insensitivity of our results on the specific magnification we are expressing our results as a function of $10/\mu$ rather than adopting a specific value.

4. Dust Content and Electron Density

We have attempted to determine the presence of dust by looking at the Balmer decrement. We measure $H\gamma/H\beta = 0.46 \pm 0.03$ as compared to the Case B recombination value of 0.47 for $T_e = 1.6 \times 10^4 \text{ K}$. This value would suggest a small $A_V = 0.12$ but is also compatible with no dust. We also find $H\delta/H\beta = 0.33 \pm 0.03$ as opposed to the Case B value of 0.26. The measured value is incompatible at $2.3+\sigma$ with dust. These conclusions are supported also by analyzing both pointings separately.

In Figure 3, we show the measured values of $H\gamma/H\beta$ and $H\delta/H\beta$ (with their 1σ error band as a function of the electron density n_e for a number of cloudy (Ferland et al. 2017) models that we have run as well as for Gutkin et al. (2016) models. The value we measure is incompatible with the presence of dust for gas temperatures below $2 \times 10^4 \text{ K}$. The absence of significant amounts of dust is also in agreement with the non-detection of far infrared continuum for this object (Hashimoto et al. 2018; Tokuoka et al. 2022).

An intriguing possibility arising from Figure 3 is that JD1 might be characterized by a higher value of the electron density than the typically assumed values in the range 100–1000. Unfortunately, our spectra cannot resolve the $[O II]$ doublet and therefore do not allow us to directly probe the electron density. As an alternative, we can derive an estimate for the electron density from the $[O III]_{\lambda 88 \mu\text{m}}/[O III]_{\lambda 5007}$ ratio. This approach has been adopted by, e.g., Fujimoto et al. (2022) for the galaxy ERO S04590 at $z = 8.5$. In order to compare the ALMA $88 \mu\text{m}$ measurement with our $[O III]_{\lambda\lambda 4959, 5007}$ measurements, we need to apply a significant aperture correction that will entail a relatively large uncertainty. We have determined an aperture correction using two different methods. The first approach is to assume that the ALMA flux is distributed across an area similar to the NIRCcam image of JD1, with which we have estimated the aperture correction factor in Section 2.2 (i.e., 2.36). Alternatively, we can derive an aperture correction by comparing the SFR derived from ALMA $[O III]_{\lambda 88 \mu\text{m}}$ to that derived from $H\beta$ (Section 3), to find an aperture correction of 1.69.¹⁶ In the following we will adopt the average of these two values and adopt as error their semi-difference, i.e., 2.02 ± 0.33 .

Armed with an estimate of the ALMA $88 \mu\text{m}$ emission, we can derive the $[O III]_{\lambda 88 \mu\text{m}}/[O III]_{\lambda\lambda 4959,5007}$ ratio as $0.055 \pm 0.012 \pm 0.009$, where the first error is the measurement 1 and the second, the aperture correction 1. We adopt the same approach as Fujimoto et al. (2022) except by using cloudy models instead of the PyNeb ones (which gives very similar results). Our cloudy models (see Section 3.2 of Oesch et al. 2007) are based on a wide variety of electron densities and use both a range of blackbody temperatures and a range of constant SFR of various metallicities modeled by GALAXEV (Bruzual & Charlot 2003).

¹⁶ A magnification gradient across JD1 would introduce a difference between the ALMA and the MIRSPEC aperture. In this paper we ignore this effect.

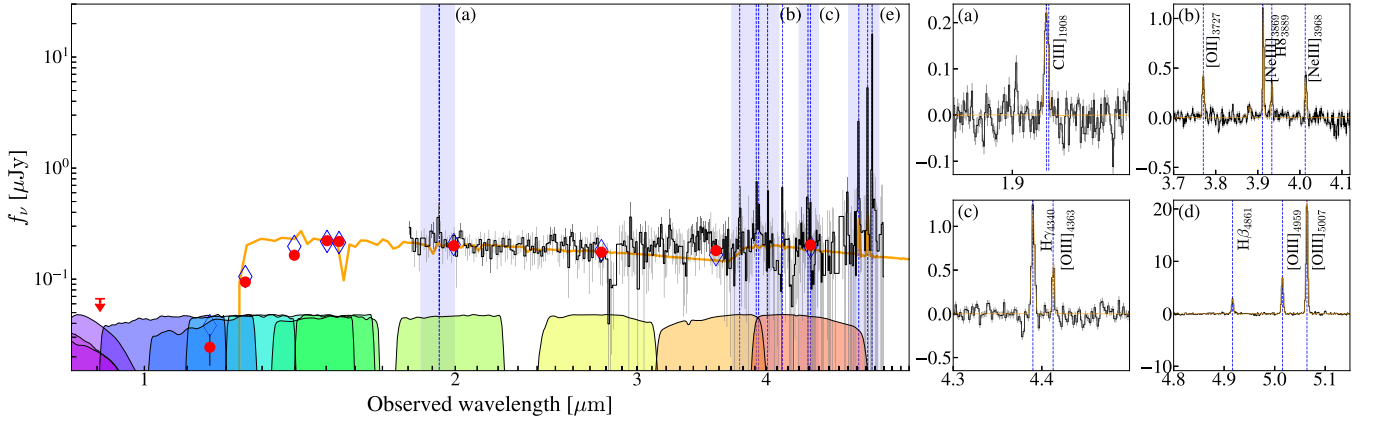


Figure 2. (Left) Spectral energy distribution of JD1 inferred by gsf (orange solid line; Section 7). Observed NIRCcam + HST photometric fluxes (red circles; inverted triangles for 2σ upper limits) and NIRSpc MSA G235M+G395M spectra (black lines) are included in the fit. Note that the observed fluxes are presented with 2σ uncertainties and not corrected for magnification. (Right) Zoomed-in plots of the continuum-subtracted spectra around strong emission lines. The blue diamonds are the fitted spectrum (orange line) convolved with the filter passbands.

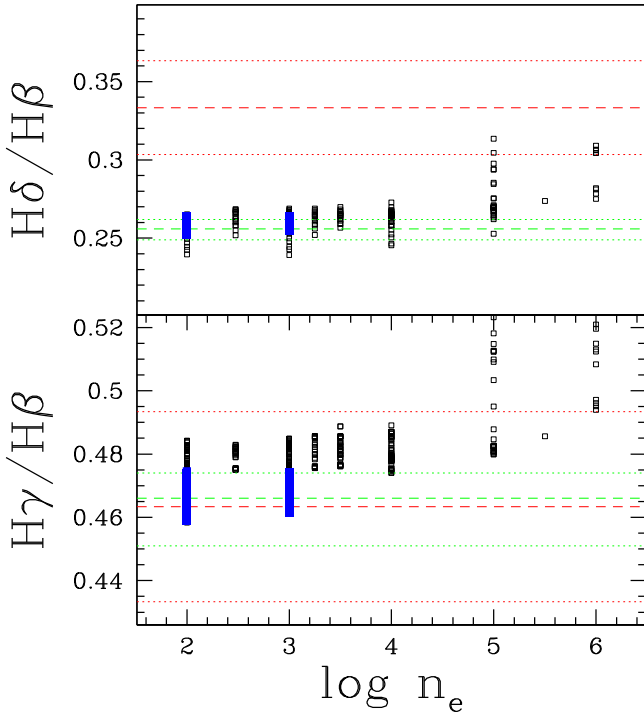


Figure 3. Ratio of $\text{H}\gamma/\text{H}\beta$ (lower panel) and $\text{H}\delta/\text{H}\beta$ (upper panel) as a function of the electron density. The red dashed line shows the measured value of the ratio for JD1 with the dotted lines showing the 1σ error bars. The green dashed line shows the Case B value of the ratio for 10^4 K, with the dotted lines showing the 5×10^3 K and 2×10^4 K Case B values. Black squares represent a multitude of cloudy models with varying properties, while the blue squares show the values for the ratio in Gutkin et al. (2016) models.

Our results are shown in Figure 4. For JD1 we find $\log n_e = 2.60^{+0.25}_{-0.27}$, or $n_e \simeq 400$. As a consistency check, for ERO S04590 we recover a value intermediate between 100 and 300 as found by Fujimoto et al. (2022).

On this basis, in the following, we assume that JD1 has a density of $n_e \simeq 400$ and no dust.

5. Emission-line Analysis

In the following, we will adopt the standard notation for line ratios, namely:

$$\text{R23} = \log([\text{O III}]\lambda\lambda 4959, 5007 + [\text{O II}]\lambda\lambda 3726, 3729)/\text{H}\beta$$

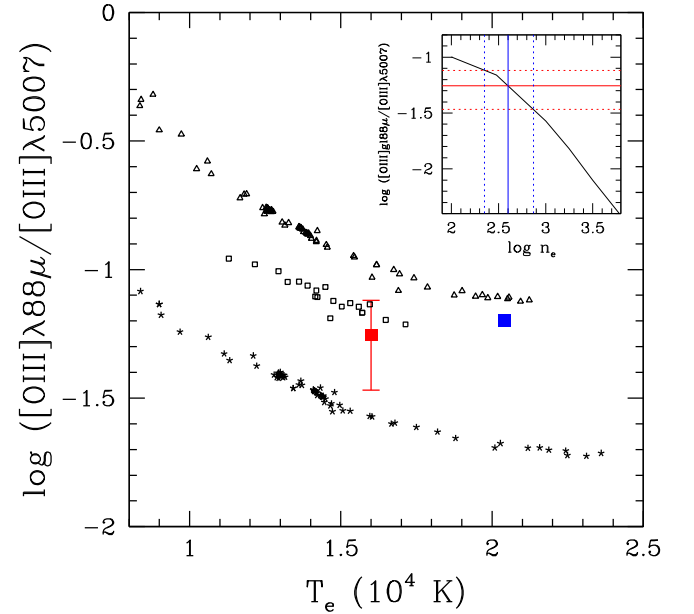


Figure 4. Ratio of $\log([\text{O III}]\lambda 88 \mu\text{m}/[\text{O III}]\lambda 5007)$ as a function of the electron temperature for a set of our cloudy models. Triangles are for $n_e = 100$, squares for $n_e = 300$, and stars for $n_e = 1000$. The red square with an error bar is for JD1 and the blue square for ERO S04590. The inset shows the change of $\log([\text{O III}]\lambda 88 \mu\text{m}/[\text{O III}]\lambda 5007)$ as a function of electron density for an electron temperature of 16,000 K. The red lines give the measured value for JD1, and its errors and the blue lines highlight the inferred values of the electron density.

$$\text{O32} = \log([\text{O III}]\lambda 5007/[\text{O II}]\lambda\lambda 3726, 3729).$$

With robust measurements of the auroral line $[\text{O III}]\lambda 4363$ and a value of the electron density, we can now apply the direct method to derive the electron temperature and the oxygen metallicity. The values derived at the two pointings are within the 1σ error bar, and thus, we will use the value from the combined spectrum. Using the Aller (1984) iterative method (see also Izotov et al. 2006) and $n_e = 400$, we derive $T_e(\text{O}^{++}) = 1.6 \times 10^4$ K and infer $12 + \log \text{O}^{++}/\text{H} = 7.88^{+0.04}_{-0.05}$. The error bars quoted here are those related to the measurement error. Varying the density between 100 and 1000 would contribute a 0.002 error. We have estimated $T_e(\text{O}^+)$ using a variety of methods (Campbell et al. 1986; Izotov et al. 2006; Pilyugin & Grebel 2016; Laseter et al. 2023;

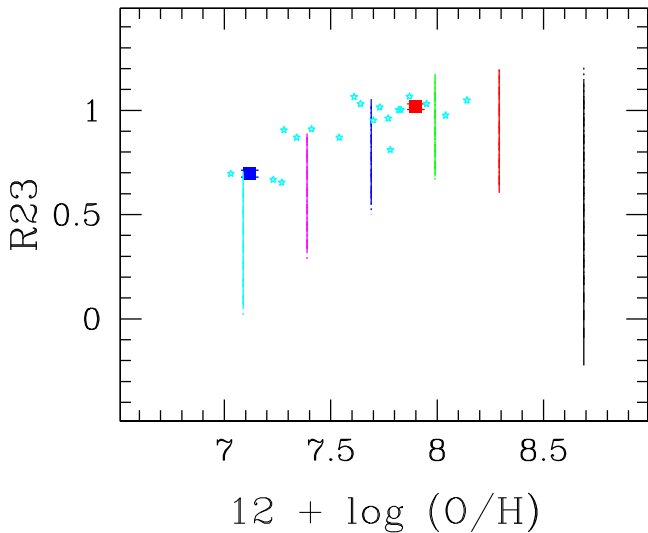


Figure 5. Direct oxygen metallicity measurement vs. the R_{23} ratio for JD1, ERO S04590 (blue) and other objects (cyan points) with auroral based measurements (Laseter et al. 2023; Nakajima et al. 2023). For reference, the vertical color lines are for Gutkin et al. (2016) models with increasing ionization parameter U from bottom to top.

Sanders et al. 2023) and find values similar to or lower than $T_e(\text{O}^{++})$. Using these values, we derive a contribution from O^+ to metallicity $12 + \log \text{O}^+/\text{H} = 6.39 - 6.55$, which is in any case small compared to the O^{++} contribution. For the total oxygen metallicity, we adopt $12 + \log(\text{O}/\text{H}) = 7.90^{+0.04}_{-0.05}$. We have also re-derived the direct metallicity for ERO S04590 and found values in agreement with the published ones.

Using the methods outlined in Izotov et al. (2006) we also derive an estimate for the neon abundance $\log(\text{Ne}/\text{H}) = -5.03 \pm 0.04$. We correct the measurement with the ionization correction factor (ICF) prescription by Amayo et al. (2021) to find $\log(\text{Ne}/\text{H}) = -5.02 \pm 0.04$ or $\log(\text{Ne}/\text{O}) = -0.69$. Our measurements suggest that JD1 is under-abundant in neon compared to solar by $\Delta \log(\text{Ne}/\text{O}) \simeq -0.23$.

We can also derive a carbon over oxygen ratio using the direct method (Aller 1984; Izotov & Thuan 1999). Here we find $\log(\text{C}^{++}/\text{O}^{++}) = -1.09$. We can compute an ICF following Berg et al. (2019). From the measured $\text{O}32 = 1.535 \pm 0.025$ and using the $Z = 0.1Z_\odot$ fit, we find $\log U = -1.647 \pm 0.026$ and a carbon ICF of 1.216 ± 0.013 . This gives us $\log(\text{C}/\text{O}) = -1.08$, implying $\Delta \log(\text{C}/\text{O}) = -0.78$ or a C/O ratio of 0.16 of the solar value.

Figure 5 compares the metallicity and the R_{23} values we derive for JD1 with those derived for other auroral line measurements from the literature (Laseter et al. 2023; Sanders et al. 2023).

In order to explore strong line diagnostics, we considered Gutkin et al. (2016) models and found that the best-fitting models correspond to 0.1 solar metallicity with $n_e = 100$ and upper mass function cutoff $m_{\text{up}} = 100M_\odot$ and the highest values of the ionizing parameter explored in the models, $U = -1.5/-1$. This is in broad agreement with the direct measurement of the oxygen metallicity. The high level of ionization is also hinted at by the very high $[\text{O III}]\lambda 5007/\text{H}\beta = 10.03 \pm 0.31$, which would correspond to the AGN–star formation boundary in the Baldwin, Phillips, & Terlevich (Baldwin et al. 1981; Lamareille et al. 2009; Lamareille 2010) diagram. Indeed, this diagram appears insufficient to separate star formation from AGN photoionization at $z \geq 6$

(Cameron et al. 2023b; Übler et al. 2023). However, we do not see any evidence of a broad component in the Balmer lines.

The measurement of (C/O) for JD1 is consistent with Gutkin’s (C/O) ~ 0.38 solar models. Thus, the broad conclusions of the direct measurements, namely that JD1 has subsolar metallicity, high ionization, and carbon under-abundance, could be derived from a strong emission-line analysis even though the details might not be precisely the same.

6. On the Nonsolar Abundance Ratio

We have seen that the direct method indicated that JD1 has C/O ratio of 0.16 the solar value. We should note the large difference in wavelength between $\text{C III}]\lambda 1909$ and $\text{H}\beta$ and the fact that they fall on different NIRSspec gratings. The measurement of (C/O) depends also on an estimation of an ionization correction based on the O32 ratio, which is itself vulnerable to the presence of dust. This opens up the possibility of uncertainties due to dust (i.e., an additional correction that we have not applied) and uncertainties in the instrumental calibration. The latter, however, should be less than 5%. Acknowledging this potential source of uncertainty, we now proceed to examine the implication of the derived under-abundance of carbon.

A similar under-abundance has been found in a galaxy at $z = 6.23$ by Jones et al. (2023). However, that galaxy has an overall lower metallicity than JD1, which may make a very young age and enrichment dominated by core-collapse supernovae less surprising. Comparing JD1 with the results by Arellano-Córdova et al. (2022), looking at the top panels of their Figure 4, one notices that JD1’s (C/O) is lower than what they find for their $z > 7$ galaxies but is not anomalous compared to $z \sim 2$ galaxies. The same is true for the (Ne/O) value of JD1, which is not observed locally for objects of its metallicity.

The under-abundance of carbon exceeds the under-abundance of neon (see Section 5). It should be noted that while a low C/O is a common feature of core-collapse supernova yields (e.g., Nomoto et al. 2013), the same is not true for (Ne/O) even though there are models where this is the case (e.g., Rauscher et al. 2002, model S20). Massive Population III PISN supernovae can also lead to significantly under-abundant (Ne/O; Heger & Woosley 2010).

7. Star Formation History and Absence of Old Stellar Populations

The sensitive photometry over $1-5 \mu\text{m}$ by NIRCcam enables us to constrain the stellar component in JD1. The F356W and F444W data points are critical as they cover, for the redshift of JD1, the rest frame $3800-4200 \text{ \AA}$ where the Balmer break, a characteristic break for relatively older (i.e., B-, A-, and F-type) stars, is located. Previous studies using Spitzer Channel (Ch1 and Ch2) reported red color ($m_{\text{ch1}} - m_{\text{ch2}} \sim 0.9 \text{ mag}$; Huang et al. 2016; Zheng et al. 2017; Hoag et al. 2018), speculating the presence of such old populations formed at $z \sim 15$ (Hashimoto et al. 2018). Here, using our JWST data, we report $m_{356} = 25.76 \pm 0.02$ and $m_{444} = 25.63 \pm 0.02$, i.e., the absence of such characteristic features in JD1. As the F356W magnitude is consistent with the previous IRAC Ch1 measurements, we suspect that image confusion might have affected the Spitzer IRAC Ch2 measurements.

The NIRC*am* photometry reveals a blue color, with $m_{F356W} - m_{F444W} = 0.13 \pm 0.01$ mag. This is considerably smaller than the previous measurement. We note that the filter curves of the corresponding bands of the two telescopes are only slightly different. For the redshift of JD1, the [O III] λ 5007 line is within the red edge of F444W but a hair outside the Spitzer Ch2. As such, the absence of strong color in F356W/F444W (despite the strong [O III] included in the redder filter) indicates the dominance of young (<100 Myr) stellar populations.

Our spectrum is deep enough to reveal the continuum and thus allows us to directly measure the Balmer break. Following the definition of Balogh et al. (1999), we measure $D(4000) \sim 0.5$, meaning that the continuum at the blue side is brighter than the red side. We also follow the procedure presented in Curtis-Lake et al. (2023) and measure the strength of the Balmer break 0.5 ± 0.1 , supporting the dominance of young populations.

Lastly, we perform a joint spectral energy distribution (SED) analysis combining photometric and spectroscopic data using `gsf` (Morishita et al. 2019). Briefly, we use `fsps` (Conroy et al. 2009), with the default MIST isochrone (Choi et al. 2016) and MILES stellar library (Falc3n-Barroso et al. 2011). Both stellar- and gas-phase metallicity are fixed to one-fifth the solar, and dust is set to zero ($A_V = 0$), based on the results from our interstellar medium analyses above. We adopt a binned star formation history, which offers flexible inference on star formation history, with a set of ages [0.001, 0.003, 0.01, 0.03, 0.1, 0.3, 0.5] Gyr. We find that JD1 experienced two distinct, major star formation phases in the past—one ~ 300 Myr old ($z \sim 14$) and a more intense one, 10 Myr old. The presence of a more recent burst is consistent with the carbon deficit that we have found in our spectral line analysis. We note that the absence of a significant amount of old stars results in a much smaller stellar mass in JD1, by a factor of $\sim \times 6.8$ from previous measurements, namely a stellar mass of $1.6_{-0.3}^{+0.3} \times 10^8 (10/\mu) M_\odot$. Combined with the SFR from Section 3, we find a specific SFR of $37_{-7}^{+10} \text{ Gyr}^{-1}$.

To check for consistency among various assumptions in SED fitting, we perform another SED analysis with BAGPIPES (Carnall et al. 2018; Hsiao et al. 2023) using BPASS v2.2.1 stellar population models (Stanway & Eldridge 2018) and CLOUDY c17.03 photoionization code (Ferland et al. 2017). We also fix the metallicities to 0.15 solar and dust to null. We assume a smooth, Gaussian process-based nonparametric star formation history (SFH; Iyer et al. 2019). We set the SFH to be controlled by four parameters: stellar mass, SFR, and two shape parameters, which essentially divide the SFH into three look-back time intervals in which the galaxy formed equal mass. The derived SFH agrees reasonably well with the binned SFH from above. The resulting stellar mass is $1.42_{-0.04}^{+0.05} \times 10^8 (10/\mu) M_\odot$. This stellar mass gives us a specific SFR of $40_{-2}^{+3} \text{ Gyr}^{-1}$.

8. Discussion and Summary

We find that JD1 is an actively star-forming galaxy characterized by metallicity about one-fifth the solar value and with emission-line ratios best explained by a very strong ionizing continuum suggestive of a very young stellar population. The youth of the object is also supported by the star formation history we derived, showing a major burst ~ 10 Myr ago, and by our finding of a low (C/O) ratio suggestive of oxygen enrichment by supernovae, while

intermediate-mass stars have not yet had the time to increase the carbon fraction. Such indications of a very active, recent, and ongoing star formation are somewhat surprising when coupled with the lack of evidence for dust as indicated by the measured Balmer decrement as well as the non-detection in the ALMA continuum reported in the literature. While geometry could conspire to give rise to gray dust (see, e.g., Witt & Gordon 1996, 2000), it is interesting that this object seems also qualitatively compatible with the dust-ejection scenario described by Ferrara et al. (2023; see also Tsuna et al. 2023). Indeed, the value of the specific star SFR we measure exceeds the value of $\sim 32 \text{ Gyr}^{-1}$ that we derive from Equation 3 of Ferrara et al. (2023). It should be noted that the complexities of how supernova-driven winds would affect the observed C/O ratio would need to be evaluated in more detail (see, e.g., Berg et al. 2019).

It is worth noticing that the (C/O) ratio of JD1, as well as its metallicity and high ionization (as inferred from the O32 ratio) are comparable to what is observed in some Green Peas galaxies at $z < 0.3$ (Ravindranath et al. 2020; Rhoads et al. 2023).

We have seen in Section 2.1 that JD1 is characterized by multiple components. This could be an indication of recent interaction or merger. However, we see no evidence of color gradients, and the line ratios at the two slightly offset slit positions are compatible. Given the absence of a color gradient, it is hard to assess how general our conclusions can be once one opens up geometry and substructure. For completeness we have also considered two-component cloudy models. The significant number of additional degrees of freedom prevents us from obtaining a unique solution but our best two-component fits share similar properties of hard ionizing flux, sometimes with AGN or an additional stellar population with 8×10^4 K of effective temperature, and oxygen-enriched models. Given the high level of degeneracy, we do not consider it useful to discuss these solutions in greater detail except to say that they are broadly compatible with the conclusions of single-component modeling.





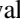




While completing this paper we were sent a pre-publication copy of a paper on JD1 by Bradač et al. (2023); we find their results broadly compatible with ours given the differences in JWST data for the two papers. Furthermore, JD1 has been observed using the NIRS*pec* Integral Field Unit by another program (PID: 1262, PI: N. Luetzgendorf), but we have currently no access to these data. It will be interesting to see whether the spatial resolved spectroscopy modifies the picture presented here and how a combined analysis of both data and of our Cycle 3 observations (#4552) aiming at observing with high resolution the rest-frame UV of JD1 will affect the picture.

Acknowledgments

This work is based in part on observations made with the NASA/ESA/CSA James Webb Space Telescope. The data were obtained from the Mikulski Archive for Space Telescopes at the Space Telescope Science Institute, which is operated by the Association of Universities for Research in Astronomy, Inc., under NASA contract NAS 5-03127 for JWST. The specific observations analyzed can be accessed via doi:[10.17909/2q9q-mw78](https://doi.org/10.17909/2q9q-mw78). These observations are associated with program JWST-GTO1199. Support for program JWST-GTO1199 was provided by NASA through grant 80NSSC21K1294. We thank S. Charlot for sharing a broader set of emission lines for the Gutkin et al. (2016) models. The authors wish to thank M. Bradač R. Ellis, A.

Ferrara, T. Hashimoto, C. Leitherer, R. Maiolino, G. Roberts-Borsani, and S. Suyu for discussions. We thank the anonymous referee for comments that helped improve the paper.

ORCID iDs

Massimo Stiavelli  <https://orcid.org/0000-0001-9935-6047>
 Takahiro Morishita  <https://orcid.org/0000-0002-8512-1404>
 Marco Chiaberge  <https://orcid.org/0000-0003-1564-3802>
 Claudio Grillo  <https://orcid.org/0000-0002-5926-7143>
 Nicha Leethochawalit  <https://orcid.org/0000-0003-4570-3159>
 Piero Rosati  <https://orcid.org/0000-0002-6813-0632>
 Stefan Schuldt  <https://orcid.org/0000-0003-2497-6334>
 Michele Trenti  <https://orcid.org/0000-0001-9391-305X>
 Tommaso Treu  <https://orcid.org/0000-0002-8460-0390>

References

- Aller, L. H. 1984, *Physics of Thermal Gaseous Nebulae* (Dordrecht: Reidel)
- Amayo, A., Delgado-Inglada, G., & Stasińska, G. 2021, *MNRAS*, **505**, 2361
- Arellano-Córdova, K. Z., Berg, D. A., Chisholm, J., et al. 2022, *ApJL*, **940**, L23
- Baldwin, J. A., Phillips, M. M., & Terlevich, R. 1981, *PASP*, **93**, 5
- Balogh, M. L., Morris, S. L., Yee, H. K. C., Carlberg, R. G., & Ellingson, E. 1999, *ApJ*, **527**, 54
- Berg, D. A., Erb, D. K., Henry, R. B. C., Skillman, E. D., & McQuinn, K. B. W. 2019, *ApJ*, **874**, 93
- Bertin, E., & Arnouts, S. 1996, *A&AS*, **117**, 393
- Böker, T., Beck, T. L., Birkmann, S. M., et al. 2023, *PASP*, **135**, 038001
- Boyett, K., Trenti, M., Leethochawalit, N., et al. 2023, arXiv:2303.00306
- Bradač, M., Strait, V., Mowla, L., et al. 2023, arXiv:2308.13288
- Bruzual, G., & Charlot, S. 2003, *MNRAS*, **344**, 1000
- Bunker, A. J., Saxena, A., Cameron, A. J., et al. 2023, *A&A*, **677**, 88
- Bushouse, H., Eisenhamer, J., Dencheva, N., et al. 2023, JWST Calibration Pipeline, v1.10.0, Zenodo, doi:10.5281/zenodo.7795697
- Cameron, A. J., Katz, H., Rey, M. P., & Saxena, A. 2023a, *MNRAS*, **523**, 3516
- Cameron, A. J., Saxena, A., Bunker, A. J., et al. 2023b, *A&A*, **677**, 115
- Campbell, A., Terlevich, R., & Melnick, J. 1986, *MNRAS*, **223**, 811
- Camall, A. C., McLure, R. J., Dunlop, J. S., & Davé, R. 2018, *MNRAS*, **480**, 4379
- Chabrier, G. 2003, *PASP*, **115**, 763
- Charbonnel, C., Schaerer, D., Prantzos, N., et al. 2023, *A&A*, **673**, L7
- Choi, J., Dotter, A., Conroy, C., et al. 2016, *ApJ*, **823**, 102
- Conroy, C., Gunn, J. E., & White, M. 2009, *ApJ*, **699**, 486
- Curti, M., D'Eugenio, F., Carniani, S., et al. 2023, *MNRAS*, **518**, 425
- Curtis-Lake, E., Carniani, S., Cameron, A., et al. 2023, *NatAs*, **7**, 622
- Falcón-Barroso, J., Sánchez-Blázquez, P., Vazdekis, A., et al. 2011, *A&A*, **532**, A95
- Ferland, G. J., Chatzikos, M., Guzmán, F., et al. 2017, *RMxAA*, **53**, 385
- Ferrara, A., Pallottini, A., & Dayal, P. 2023, *MNRAS*, **522**, 3986
- Finney, E. Q., Bradač, M., Huang, K.-H., et al. 2018, *ApJ*, **859**, 58
- Fujimoto, S., Ouchi, M., Nakajima, K., et al. 2022, arXiv:2212.06863
- Fukugita, M., Ichikawa, T., Gunn, J. E., et al. 1996, *AJ*, **111**, 1748
- Grillo, C., Karman, W., Suyu, S. H., et al. 2016, *ApJ*, **822**, 78
- Gutkin, J., Charlot, S., & Bruzual, G. 2016, *MNRAS*, **462**, 1757
- Hashimoto, T., Laporte, N., Mawatari, K., et al. 2018, *Natur*, **557**, 392
- Heger, A., & Woosley, S. E. 2010, *ApJ*, **724**, 341
- Heintz, K. E., Giménez-Arteaga, C., Fujimoto, S., et al. 2023, *ApJL*, **944**, L30
- Hoag, A., Bradač, M., Brammer, G., et al. 2018, *ApJ*, **854**, 39
- Home, K. 1986, *PASP*, **98**, 609
- Hsiao, T. Y.-Y., Coe, D., Abdurro'uf, et al. 2023, *ApJL*, **949**, L34
- Huang, K.-H., Bradač, M., Lemaux, B. C., et al. 2016, *ApJ*, **817**, 11
- Iyer, K. G., Gawiser, E., Faber, S. M., et al. 2019, *ApJ*, **879**, 116
- Izotov, Y. I., Stasińska, G., Meynet, G., Guseva, N. G., & Thuan, T. X. 2006, *A&A*, **448**, 955
- Izotov, Y. I., & Thuan, T. X. 1999, *ApJ*, **511**, 639
- Jdox 2016, JWST User Documentation (JDOX), JWST User Documentation Website, <https://jwst-docs.stsci.edu/>
- Jones, T., Sanders, R., Chen, Y., et al. 2023, *ApJL*, **951**, L17
- Kelly, P. L., Diego, J. M., Rodney, S., et al. 2018, *NatAs*, **2**, 334
- Lamareille, F. 2010, *A&A*, **509**, A53
- Lamareille, F., Brinchmann, J., Contini, T., et al. 2009, *A&A*, **495**, 53
- Laseter, I. H., Maseda, M. V., Curti, M., et al. 2023, arXiv:2306.03120
- Lotz, J. M., Koekemoer, A., Coe, D., et al. 2017, *ApJ*, **837**, 97
- Maiolino, R., Uebler, H., Perna, M., et al. 2023, arXiv:2306.00953
- Morishita, T., Abramson, L. E., Treu, T., et al. 2019, *ApJ*, **877**, 141
- Morishita, T., Roberts-Borsani, G., Treu, T., et al. 2023a, *ApJL*, **947**, L24
- Morishita, T., & Stiavelli, M. 2023, *ApJL*, **946**, L35
- Morishita, T., Stiavelli, M., Chary, R.-R., et al. 2023b, arXiv:2308.05018
- Nakajima, K., Ouchi, M., Isobe, Y., et al. 2023, arXiv:2301.12825
- Nomoto, K., Kobayashi, C., & Tominaga, N. 2013, *ARA&A*, **51**, 457
- Oesch, P. A., Brammer, G., van Dokkum, P. G., et al. 2016, *ApJ*, **819**, 129
- Oesch, P. A., Stiavelli, M., Carollo, C. M., et al. 2007, *ApJ*, **671**, 1212
- Oke, J. B., & Gunn, J. E. 1983, *ApJ*, **266**, 713
- Pilyugin, L. S., & Grebel, E. K. 2016, *MNRAS*, **457**, 3678
- Postman, M., Coe, D., Benítez, N., et al. 2012, *ApJS*, **199**, 25
- Rauscher, T., Heger, A., Hoffman, R. D., & Woosley, S. E. 2002, *ApJ*, **576**, 323
- Ravindranath, S., Monroe, T., Jaskot, A., Ferguson, H. C., & Tumlinson, J. 2020, *ApJ*, **896**, 170
- Rhoads, J. E., Wold, I. G. B., Harish, S., et al. 2023, *ApJL*, **942**, L14
- Sanders, R. L., Shapley, A. E., Topping, M. W., Reddy, N. A., & Brammer, G. B. 2023, arXiv:2303.08149
- Stanway, E. R., & Eldridge, J. J. 2018, *MNRAS*, **479**, 75
- Steinhardt, C. L., Jauzac, M., Acebron, A., et al. 2020, *ApJS*, **247**, 64
- Tacchella, S., Eisenstein, D. J., Hainline, K., et al. 2023, *ApJ*, **952**, 74
- Tokuoka, T., Inoue, A. K., Hashimoto, T., et al. 2022, *ApJL*, **933**, L19
- Treu, T., Schmidt, K. B., Brammer, G. B., et al. 2015, *ApJ*, **812**, 114
- Tsuna, D., Nakazato, Y., & Hartwig, T. 2023, arXiv:2309.02415
- Übler, H., Maiolino, R., Curtis-Lake, E., et al. 2023, *A&A*, **677**, 145
- Witt, A. N., & Gordon, K. D. 1996, *ApJ*, **463**, 681
- Witt, A. N., & Gordon, K. D. 2000, *ApJ*, **528**, 799
- Zheng, W., Postman, M., Zitrin, A., et al. 2012, *Natur*, **489**, 406
- Zheng, W., Zitrin, A., Infante, L., et al. 2017, *ApJ*, **836**, 210